Efficient Deoxygenation of Palm Oil to Green Diesel Using a Metal Oxide Catalysts Supporting on ZrO_2-Enhanced Graphene Oxide

Attared F. Hassan[1], Hassan T. Abdulsahib[1], Faris A. J. Al-Doghachi[1,*], and Yun Hin Taufiq-Yap[2,3,*]

[1]*Department of Chemistry, College of Science, University of Basrah, 61004, Basrah, Iraq.*

[2]*Catalyst Science and Technology Research Center, Faculty of Science, University Purta Malaysia, 43400, UPM Serdang, Selangor, Malaysia.*

[3]Institute of Plantation Studies, Universiti Putra Malaysia, 43400, UPM Serdang, Selangor, Malaysia.

* *Corresponding Author. E-mail: faris.jassim@uobasrah.edu.iq*

Abstract

NiO, Fe_2O_3, and bimetallic oxide $NiFe_2O_4$ catalysts supported on graphene oxide and promoted with ZrO_2 were synthesized via wet-impregnation approach. A systematic characterization of the catalysts physicochemical properties was evaluated using X-ray diffraction (XRD), Thermogravimetric analysis (TGA), Fourier Transform Infrared (FTIR), Temperature -programmed desorption CO_2 (TPD-CO_2), Brunaur-Emmett-Teller (BET) surface area, Field emission Scanning electron microscopy (FESEM), and Transmission electron microscopy (TEM) analysis. The catalysts were evaluated as heterogeneous catalysts in the deoxygenation (DO) of palm oil for green diesel production under varying operating conditions. Among the catalysts tested, Fe_2O_3/ZrO_2-GO (calcined at 400 °C for 4 h, 5 wt% loading) demonstrated superior catalytic activity, achieving a maximum hydrocarbon yield (HC%) of 98.0%, bio-jet fuel (BJF) selectivity of 40%, and kerosene yield of 86%. The exceptional performance is attributed to the catalyst's large BET surface area (18.64 m^2/g), substantial pore volume (0.027 cm^3/g), and moderate surface basicity (3234.65 µmol/g), which collectively facilitate efficient deoxygenation via decarboxylation (DCO_2) and decarbonylation (DCO) pathways while suppressing undesired cracking. Furthermore, the catalyst exhibited remarkable stability and reusability over four consecutive reaction cycles, retaining 92% hydrocarbon yield and 80.9% kerosene

yield, with BJF selectivity increasing to 84%. The gradual decline in performance is attributed to carbon deposition (coke formation), pore blockage, and sintering-induced degradation of the mesoporous network, as confirmed by post-reaction XRD and BET analysis.

Keywords:

Renewable diesel, metallic oxide, Deoxygenation, Bio-Jet-Fuel, Graphene oxide.

1. Introduction

Green diesel is known as a second-generation biodiesel made from renewable sources like animal fats, vegetable oils. It is consisting of straight chain and branched alkanes, allowing it to be used as a drop-in fuel in any diesel engine without blending limits or modification, it has properties such as a high cetane number, low sulfur and aromatic content, elevated heating value, better oxidation stability, and longer storage life [1]. Green diesel production from vegetable oils and fatty acids through catalytic deoxygenation DO reaction by removing carbon dioxide CO_2 and CO via decarboxylation (DCO_2), decarbonylation (DCO) producing n-alkane and n-alkene as major product and H_2O as bi-product [2]. The efficiency of this process is influenced by the type of catalyst and its support material as well as the operating conditions employed [3]. Catalysts investigated for DO can be classified into four main groups: (i) noble metals (Pt-group: Pd, Pt, Au, Rh, Ru) [4-6], which exhibit high intrinsic activity but are restricted by high cost and limited availability; (ii) bimetallic catalysts [7], which leverage synergistic effects to improve activity and stability; iii) metal-based compounds including metal oxides [8], nitride [9], carbides [10,11], sulfides [12], and phosphides [13] which have demonstrated effectiveness in promoting DO reactions; and (iv) transition metals (Ni, Cu. Fe, Co, W, Mo) [7,14-18], which offer low-cost alternatives with satisfactory performance. Beyond the active metal phase, the choice of catalyst support critically determines catalytic performance through its influence on metal dispersion, surface area, pore structure, thermal stability, and acid–base properties. Supports are generally classified into four categories: solid acids (Zeolites) [19], reducible oxides (ZrO_2, TiO_2, CeO_2) [20-22], refractory oxides (SiO_2, Al_2O_3) [2,23], and carbon-based materials (graphene, fullerenes, activated carbon, carbon nanotubes) [5,13,24]. These support catalysts have been widely used in green diesel production due to their role of enhancing the

activity and stability of the catalyst and reducing deactivation. It has attracted increasing attention for designing advanced functional material. Graphene with its ultrathin structure and hexagonal sp^2 lattice, stand out among them. Graphene oxide (GO) is produced from oxidation of Graphite, which is reduced chemically or thermally into nanosheets. The abundant of oxygen functional groups on the surface and edges of Graphene oxide serve as enhancing sites for nanoparticles hybrids. However, Graphene tendency to agglomerate due to Vanderwal's interactions, which can be mitigated by organic modifiers or revers micelles' which help stabilize the material and act as micro-reactors for immobilizing noble metal ions [25].

This study investigates the synthesis of NiO, Fe2O3, and NiFe2O4 catalysts supported on a ZrO2-GO composite and evaluates their performance in the DO of palm oil for green diesel and bio-jet fuel production. The aim of this work lies in the usage of ZrO2 promoted GO as a bifunctional support that simultaneously provides structural stability, high surface area, and tunable acid-base properties, while systematically comparing mono and bimetallic oxides on the physicochemical properties and catalytic performance of the ZrO2-GO support. The reusability and deactivation behavior of the optimal catalyst are also investigated in depth.

2. Materials and Methods

2.1 Materials

Palm oil was obtained from Malaysia (Selangor), and used for DO reaction without further treatment. $Ni(NO_3)_2.6H_2O$ (H&W; > 99%), $Fe((NO_3)_3.9H_2O$ (RDH; > 99%), $NaNO_3$ (Merck; > 99%), H_2SO_4, $KMnO_4$, and Graphite with 99% purity was supplied by Merck (Germany), $ZrCl_4$ anhydrous (Merck; 99%). All chemicals were used without any treatment.

2.2 Methods

2.2.1 Preparation of Graphene oxide (GO) Via modified Hummer's method

Graphite powder (2g) was mixed with conc. H2SO4 (46mL) and NaNO3 (1g) in 500 mL flask and then placed in an ice bath (0-5 oC) under vigorous magnetic stirring. After about approximately 15 min, potassium permanganate KMNO4 (6g) was added gradually to the suspension in about 90 min with stirring to keep the reaction temperature below 20 oC. During this process, the solution turned dark green. The mixture was then stirred for 2 h and subsequently maintained at 35 °C for 30 min.

Deionized water (100 mL) was slowly added, and the reaction temperature was increased to 98 °C, with continuous stirring for 30 min. After an additional 15 min, the mixture was further diluted to a total volume of approximately 208 mL using hot deionized water. Next, 20 mL of 30% H_2O_2 was added dropwise to eliminate residual $KMnO_4$ and MnO_2, resulting in a dark brown solution. The suspension was stirred overnight at ambient temperature, then filtered and washed multiple times with deionized water until a neutral pH was reached. Finally, the product was dried under vacuum at 50 °C until a constant weight was obtained [26].

2.2.2 Synthesis of ZrO_2-GO support catalyst

ZrO2-GO support catalyst was synthesized via a wet-impregnation method as reported previously [27]. Graphene oxide (80 wt%) was dispersed in deionized water in a 250 mL beaker. Subsequently, an aqueous solution containing 20 wt% $ZrCl_4$ was added to the GO suspension. The resulting mixture was stirred under gentle heating for 4 h to ensure proper mixing. The mixture was then dried overnight at 80 °C, followed by calcination at 400 oC for 4 h with heating rate of 5 oC/min (Scheme 1).

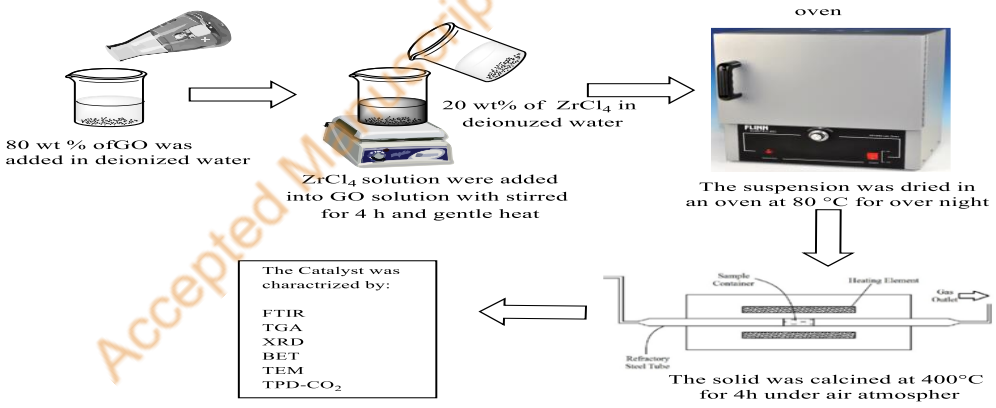

Scheme 1. Preparation of ZrO_2-GO support catalyst

2.2.3 Synthesis of MO/ ZrO_2-GO catalyst

5wt% NiO was introduced via wet impregnation using nickel nitrate hexahydrate Ni(NO3)2.6H2O as the precursor. The appropriate amount of nickel nitrate was dissolved in deionized water and added to a suspension containing 95 wt% ZrO2-GO. The mixture was stirred under gentle heating for 4 h to ensure uniform dispersion.

The resulting suspension was dried overnight at 80 °C and then calcined at 400 °C for 4 h with a heating rate of 5 °C/min (Scheme 2). The Fe2O3/ZrO2-GO catalyst was synthesized following the same procedure, using iron nitrate nonahydrate ($Fe(NO_3)_3 \cdot 9H_2O$) as the precursor.

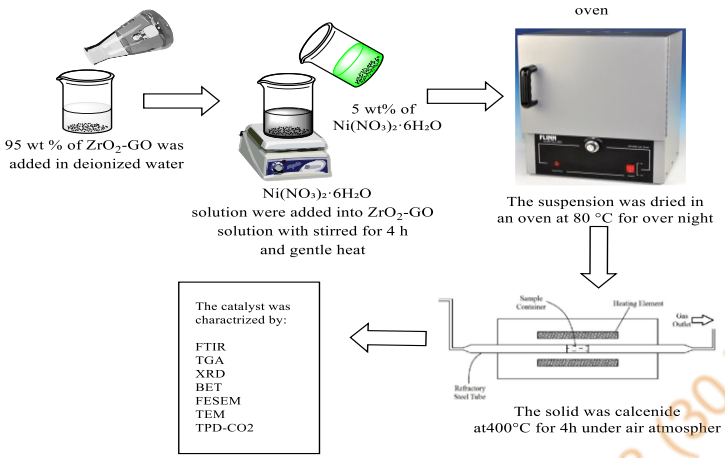

Scheme 2. Synthesis of NiO/ZrO_2-GO catalyst

2.2.4 Synthesis of $NiFe_2O_4$/ ZrO_2-GO catalyst

Aqueous solutions containing 5wt% Ni(NO3)2.6H2O and 5wt% Fe((NO3)3.9H2O were prepared and added to aqueous solution of 90 wt% of ZrO2-GO. The mixture was stirred under gentle heating for 4 h, followed by drying at 80 °C overnight. Finally, the dried sample was calcined at 400 °C for 4 h with a ramping rate of 5 °C/min.

2.3 Deoxygenation reaction of Palm oil

Deoxygenation (DO) of palm oil was carried out in 250 mL semi-batch reactor using 9.8 g of palm oil and 0.2 g of catalyst. The reaction was conducted at 350 oC for 3 h. under a constant N2 flow of 40 mL/min. During the reaction, volatile products were condensed into a liquid deoxygenated fraction using an external water-cooling circulator maintained at 15 °C and collected in a receiving flask. The composition of the deoxygenated products was analyzed by Gas chromatography with flame ionization detection (GC-FID), and Gas Chromatography- Mass Spectrometry (GC-MS).

2.4 Product Characterization

For quantitative analysis, the deoxygenated liquid samples were analyzed by Gas

chromatography with flame ionization detection (GC-FID) and compared against a standard containing C_8 - C_{35} alkane mixtures. Prior to injection, the DO liquid sample were diluted in GC- grade hexane employed as an internal standard. Analysis was performed on a SHIMADZU GC-14B system equipped with an- Hp-5 capillary column (30 m x 0.32 mm). A 1µL aliquot of each sample was injected into a front inlet set at 250 ^oC. The detector temperature was maintained at 300 ^oC [27]. The oven temperature program was initial at 40 ^oC (held for 6 min.), followed by a ramp of 7 ^oC/min to a final temperature of 270 ^oC, under N_2 carrier gas flow. Hydrocarbon yield, Kerosene yield, and bio jet fuel BJF selectivity were calculated based on Equation (1), (2), and (3) [27].

$$\text{Hydrocarbon yield (\%)} = \frac{\sum Area\ of\ alkane(C8-C20)+\sum Areaof\ alkene(C8-C20)}{\sum Area\ of\ the\ product} \text{ X } 100\% \qquad \text{Eq (1)}$$

$$\text{Kerosene yield (\%)} = \frac{\sum Area\ of\ alkane\ (C8-C16)+\sum Area\ of\ alkene(C8-C16)}{\sum Area\ of\ the\ product} \text{ X } 100\% \qquad \text{Eq (2)}$$

$$\text{BJT selectivity (\%)} = \frac{\sum Total\ area\ of\ alkane\ \&\ alkene\ (C11+C13+C15)}{\sum Area\ of\ alkane(C8-C20)+\sum Area\ of\ alkene\ (C8-C20)} \text{X } 100\% \qquad \text{Eq (3)}$$

A SHIMADZU QP2010 plus GC-MS instrument equipped with a Zebron ZB-5 MS column (30 m x 0.25 mm x 0.25 µm) and a splitless inlet was employed to identity the organic components in the DO products. The liquids were diluted to 100 ppm in n-hexane (≥98% purity), and the detected compounds were compared with the National Institute of standards and Technology (NIST) Library [28]. The selectivity of the DO products was calculated according to equation (4):

$$S_{product\ \%} = \frac{Cy}{\sum ny} \text{ X } 100\% \qquad \text{Eq (4)}$$

Where $S_{product}$ represent the selectivity of the products component (%), Cy is the peak area of the identified compound, and ∑ny is peak area of all organic products.

2.5 Optimization study using the one-variable-at-a-time (OVAT) technique

The reaction conditions for the best-performing catalyst were optimized using the one-variable-at-a-time (OVAT) approach. To establish the optimum reaction conditions, temperature (270-370 oC) and reaction time (2-6 h), and catalyst loading (1, 3, 5, 7, and 10 wt%) were systematically varied under a constant N2 atmosphere

at 400 rpm. The resulting liquid products were analyzed by GC-FID, and the conditions that produced the maximum hydrocarbon yield were identified as the optimum operating parameters via this method.

2.6 Reusability and stability of new catalyst

The catalyst was further examined for reusability and long -term stability at optimized reaction conditions. Reusability tests were performed using the spent catalyst was separated from the reaction mixture, thoroughly washed within n-hexane several times to remove residual polar and non-polar compounds, and then dried at 100 ^{o}C for 4 h before reused in the subsequent DO reaction. The hydrocarbon yield HC%, Kerosene fraction, and product selectivity were calculated according to Equations (1), (2), and (3). This procedure was repeated across successive reaction cycles. In addition, the spent catalyst was characterized by XRD, TEM, and BET to assess its structural and physicochemical properties, while the deoxygenated liquid product from each cycle were analyzed using GC-FID.

3. Results and discussion

The crystallographic structures of the newly synthesized catalysts were examined by XRD over the 2θ range 5-80°. The identification of diffraction peaks was carried out with reference to International Centre for Diffraction Data (ICDD). The corresponding XRD pattern of the catalysts are illustrated in Fig. 1. Whereby the XRD results for all catalysts displayed a diffraction peak at 2 θ = 26.5o (d-spacing ~3.36AO) is characteristic of the (0 0 2) plane of graphitic carbon, indicating the presence of partially thermal reduced graphene oxide (rGO) or a graphitic structure with restored sp2 carbon domains (ICDD PDF # 00-041-1487) [28].

The XRD pattern clearly indicates the presence of a mixed-phase zirconia system, containing both monoclinic m-ZrO2, and tetragonal t-ZrO2 polymorphs. The peak at 2θ = 28.29° (110) is the fingerprint of m-ZrO2, while the peak at 2θ = 30.86° (101) is the most intense reflection for t-ZrO2 (ICDD PDF #01-179-1765). Additional peaks at 2θ = 40.5° (-1 0 2) and 50.18 (2 2 0) attributed to m-ZrO2 (ICDD PDF # 00-037-1484), while the composite peak at 2θ = 50.18° also contains contributions from t-ZrO2 (200) and (112) planes [29,30].

The ZrO_2-GO support catalyst exhibited peaks at 2θ =17.97^{o}, 23.8^{o}, and 25.67^{o} which

are usually associated with presence of GO, with an expanded d-spacing (1.259, 0.098, and 1.259 A°) respectively compared to pure graphite which confirms presence of oxygen-containing functional groups, and also showed peaks at 37.11° and 43.37° may be correspond to the (1 0 2) and (1 1 2) planes of t-ZrO_2 respectively (ICDD PDF #01-179-1765) [28,29].

The NiO/ZrO_2-GO catalyst exhibited peaks at 2θ = 43.30°, 58.64° and 73.70° correspond to (2 0 0), (2 2 0), and (3 1 1) planes indicate the presence of cubic NiO, (ICDD PDF #00-089-7390) [31]. The Fe_2O_3/ZrO_2-GO catalyst showed the most characteristic peaks of hematite at 2θ = 35.70° corresponding to (1 0 4) plane [8]. The peaks at 2θ = 37.18°, 43.4° 58.74o, and 66.74° correspond to (1 1 0), (2 0 0), (1 1 6), and (2 1 4) planes of hematite, providing strong confirmation for this phase, (ICDD PDF #01-089-0596) (Hematite) [32]. The NiO/ZrO_2-GO and Fe_2O_3/ZrO_2-GO catalysts exhibited peak at 2θ = 21.30° may be attributed to a less ordered structure of GO.

$NiFe_2O_4$/ ZrO_2-GO catalyst displayed a diffraction peak at 2 θ = 6.7° correspond to very large d-spacing (13.2A°), which is characteristic of the (0 0 1) plane of fully oxidized GO with extensive oxygen-containing functional groups (ICDD PDF #00-041-1487) [8]. The presence of cubic spinel nickel ferrite ($NiFe_2O_4$) is confirmed its characteristic peaks: The peaks at 2θ = 30.81°, 43.37°, and 57.8° is typical for spinel ferrite [8]. The peaks at 2θ = 45.88°, and 47.9° likely correspond to (4 0 0) and (3 3 1) planes of $NiFe_2O_4$ respectively. The peaks at 2θ = 66.50°, and 73.60° can be assigned to (4 4 0) and (5 3 3) planes of $NiFe_2O_4$ (ICDD PDF #01-086-2267) for $NiFe_2O_4$ [33].

The Debye-Scherrer equation was employed to estimate the crystallite sizes of the catalysts based on the most intense peaks in their XRD patterns. The calculated crystallites sizes were (48.2, 19.4, 17.8, and 21) nm for ZrO_2-GO, NiO/ZrO_2-GO, Fe_2O_3/ZrO_2-GO, and $NiFe_2O_4$/ ZrO_2-GO catalysts, respectively. The smaller crystallite size of Fe2O3/ZrO2–GO reflects a higher degree of metal dispersion, which directly contributes to a greater number of accessible active sites and is consistent with its superior catalytic activity.

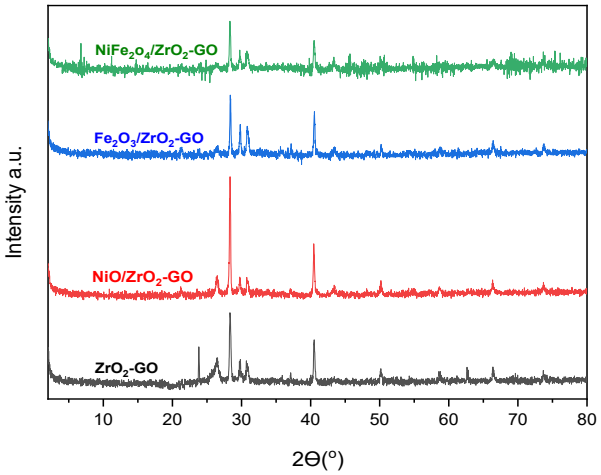

Figure 1. XRD pattern of the catalysts.

The N_2 adsorption–desorption isotherms of all catalysts (Figure 2) exhibited Type IV isotherms according to IUPAC classification, confirming mesoporous character with slit-like pores typical of graphene-based supports. The BET surface area, pore volume, and average pore diameter are summarized in Table 1. The Fe_2O_3/ZrO_2-GO catalyst exhibited the highest BET surface area (18.64 m^2/g) and pore volume (0.027 cm^3/g) among all catalysts, directly reflecting superior metal dispersion and accessibility. The relatively small average pore diameter (4.305 nm) falls within the mesoporous regime, which is optimal for the adsorption and diffusion of fatty acid triglyceride molecules (kinetic diameter ~ 2-3 nm for fatty acid chains). The combination of high surface area and adequate pore size facilitates efficient mass transfer of both reactants and products during the DO reaction, thereby enhancing overall catalytic activity [3]. The high surface area is consistent with the small crystallite size of Fe_2O_3 (17.8 nm), confirming finely dispersed active phase on the ZrO_2-GO support.

In contrast, NiO/ZrO_2-GO exhibited the lowest surface area (7.14 m^2/g), suggesting that NiO deposition caused significant pore blockage during impregnation. Although its larger average pore diameter (7.427 nm) may allow molecular diffusion, the reduced number of accessible active sites limits overall activity. $NiFe_2O_4/ZrO_2$-GO showed a moderate surface area (14.77 m^2/g) but the lowest pore volume (0.0188 cm^3/g), indicating that co-impregnation with both Ni and Fe partially fills the pore network, reducing permeability while maintaining reasonable site dispersion.

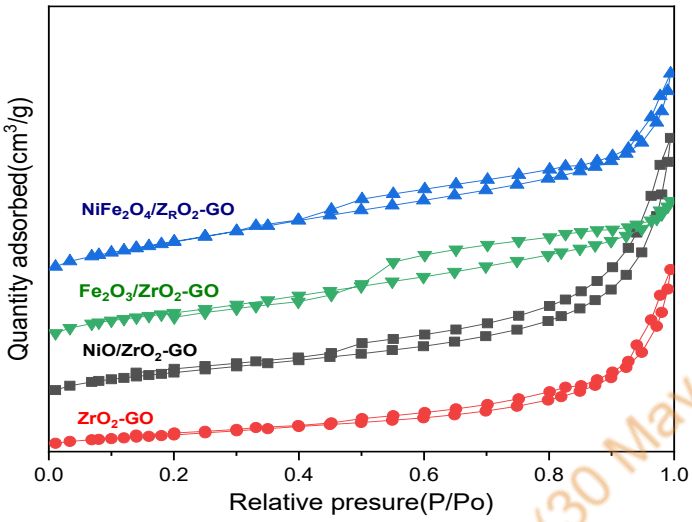

Figure 2. Isotherm linear plot for newly synthesized catalysts.

Table 1. N_2- adsorption/desorption analysis for new catalysts.

Catalyst	**N_2 adsorption-desorption analysis**		
	Surface Area (m^2/g)	**Pore size diameter (nm)**	**Pore volume (cm^3 / g)**
ZrO_2-GO	14.646	5.783	0.0212
NiO/ZrO_2-GO	7.143	7.427	0.0228
Fe_2O_3/ZrO_2-GO	18.64	4.305	0.027
$NiFe_2O_4$/ ZrO_2-GO	14.77	4.499	0.0188

The FTIR spectra of all catalysts reveal a characteristic absorption band confirming the coexistence of metal oxides with thermal reduced of graphene oxide, the diminished oxygen-containing bands (C=O, C-O) demonstrate partial thermal reduction of GO during calcination process, while the strong M-O vibrations confirm successful incorporation of Ni, Fe, and Zr oxides as shown in Fig. 3. The FTIR spectra displayed Absorption bands near 1634 cm cm^{-1} assigned to O-H bending confirming adsorbed moisture. The band at 1566 cm^{-1} corresponds to C=C stretching vibration [34]. The band in range 1367-1214 cm^{-1} indicate C-O stretching vibration of epoxy groups, However, the reduced intensity of these bands compared to pristine GO

suggests thermal reduction of graphene oxide (rGO) during calcination. Bands in the 1106-977 cm^{-1} region are assigned to alkoxy C-O stretching, while strong bands in the 835-440 cm^{-1} region correspond to M-O stretching vibrations (Ni-O, Fe-O, Zr-O), confirming successful incorporation of NiO, Fe_2O_3, and ZrO_2 into the support framework [8,31,33,35].

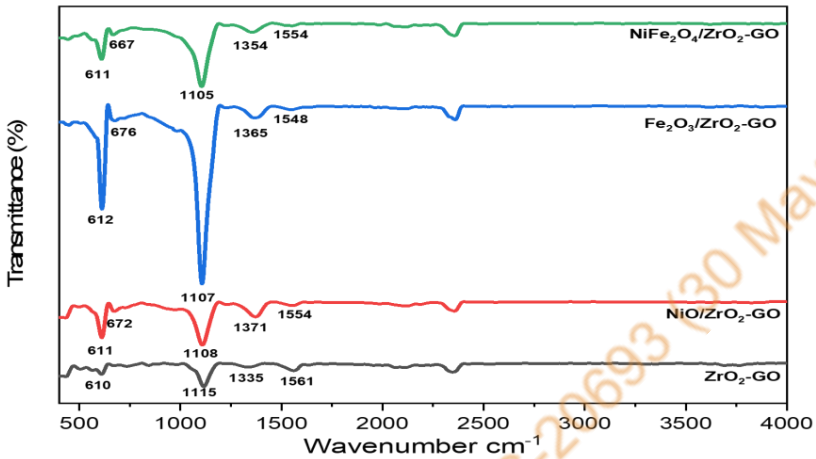

Figure 3. FTIR spectra for all new catalysts.

The surface basicity of the catalysts was evaluated by TPD-CO_2 (Figure 4, Table 2), as basicity plays a critical role in deoxygenation pathways. Basic sites facilitate the activation of the carboxyl group in fatty acids and promote C-O bond cleavage via DCO_2 and DCO pathways, whereas excessively strong basic sites can catalyze undesired condensation and cracking reactions. Therefore, a moderate density of basic sites is optimal for selective deoxygenation to diesel-range hydrocarbons [36,37].

All catalysts displayed CO_2 desorption peaks at temperatures >600 °C, classified as strong basic sites associated with low-coordination O^{2-} species [37]. The Fe_2O_3/ZrO_2-GO catalyst showed three desorption peaks at 290°C (weak), 609 °C (moderate), and 950°C (strong), indicating a distribution of basic site strengths. Importantly, it exhibited the lowest total basicity among the catalysts (3234.65 µmol/g). This moderate basicity is mechanistically significant: sufficient to activate C-O bonds and promote DCO_2/DCO pathways, yet mild enough to suppress secondary cracking and condensation reactions that would otherwise reduce hydrocarbon yield and selectivity [41,42]. The presence of weak and moderate sites also suggests hydroxyl groups (-OH) and Lewis acid-base pairs on the ZrO_2 surface contribute to the broad basicity distribution.

In contrast, NiO/ZrO_2-GO had the highest basicity (7273.3 µmol/g), which correlates with its lower catalytic performance. Excessively strong basic sites promote over-activation of the substrate, leading to undesired cracking and condensation products rather than selective C_{15}-C_{17} hydrocarbons. This mechanistic link between basicity and selectivity is clearly demonstrated by comparing the catalytic performance of NiO/ZrO_2-GO (lowest HC% and kerosene yield) with Fe_2O_3/ZrO_2-GO (highest HC% and kerosene yield) although the former possesses almost double the basic site density compared to the latter.

Table 2. TPD-CO_2 basicity data for the synthesized catalysts.

TPD-CO_2		
Catalyst (µmol/g)	CO_2- desorption temperature (°C)	Amount of CO_2- desorbed
ZrO_2-GO	861	6018.42
NiO/ZrO_2-GO	900	7273.3
Fe_2O_3/ZrO_2-GO	290, 609, 950	3234.65
$NiFe_2O_4$/ZrO_2-GO	828	6618.399

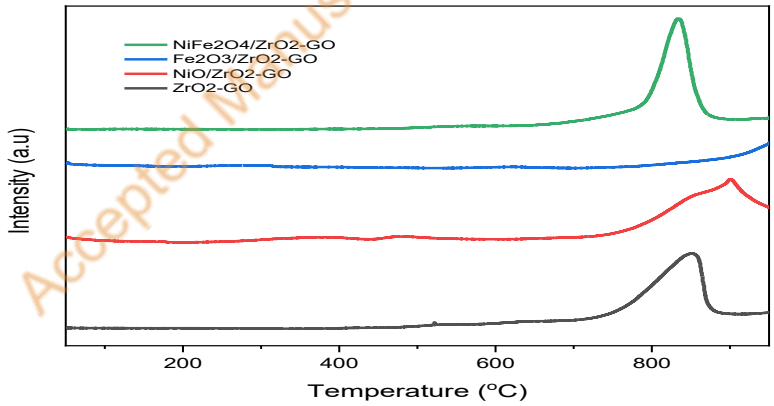

Figure 4. Basicity profiles for new catalysts.

TEM micrographs (Figure 5a–d) reveal the morphological features of the synthesized catalysts. The TEM image of ZrO_2-GO catalyst shows thin, wrinkled rGO nanosheets supporting well-dispersed, angular ZrO_2 nanoparticles forming small semi-agglomerated clusters without significant overgrowth, confirming strong anchoring

of ZrO_2 on the GO surface.

In the metal oxide-loaded catalysts, the active oxide nanoparticles (NiO, Fe_2O_3) appear as compact, angular grains forming densely packed clusters with high electron density, embedded within brighter ZrO_2 promoter domains. The faint, translucent backgrounds confirm effective anchoring of all nanoparticles onto thin GO nanosheets. For Fe_2O_3/ZrO_2-GO, the fine dispersion of Fe_2O_3 nanoparticles on the mesoporous support creates an extensive interfacial area between the active phase and the support. This morphology promotes electron transfer and facilitates the interaction of fatty acid molecules with active Fe^{3+} sites during DO, consistent with the superior catalytic activity of this catalyst. These microstructural features directly correlate with the high BET surface area and pore volume observed for Fe_2O_3/ZrO_2-GO.

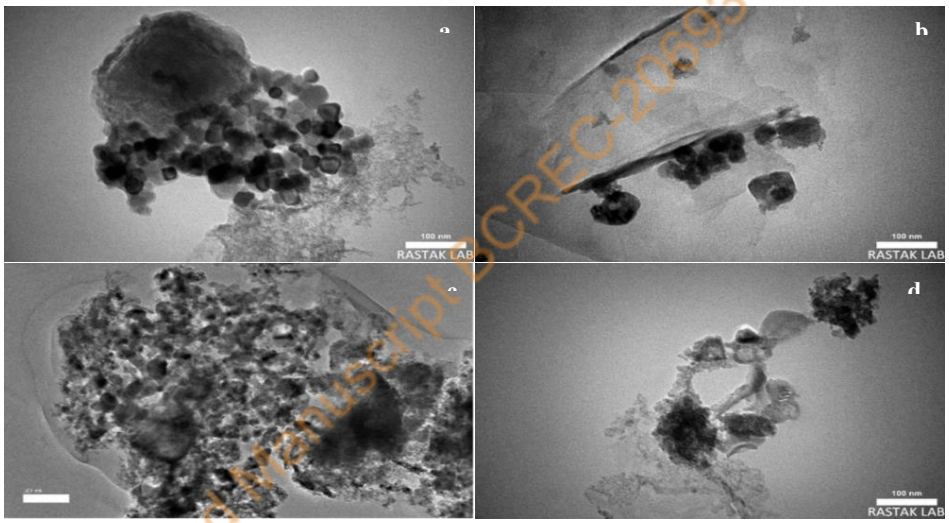

Figure 5. TEM image of (a) ZrO_2 -GO, (b) NiO/ZrO_2 -GO, (c) Fe_2O_3/ZrO_2-GO, (d) $NiFe_2O_4$/ ZrO_2-GO catalyst.

The thermal resistance of the newly synthesized catalysts was examined by TGA analysis, which calculate the weight loss of catalysts as increasing the temperature from ambient temperature to 1000 ^oC under nitrogen atmosphere, and the corresponding results are presented in Figure 6. As shown in Figure 6, all catalysts revealed three distinct decomposition stages. The first stage occurring between approximately ~ 55-370 ^oC involved a weight loss about 5-20% attributed to desorption of physiosorbed water molecules and removal of labile oxygen containing groups on the surface of graphene oxide (-COOH, -CO, -OH, epoxy) [26]. The second

stage in the range (370-716 °C) showed a weight loss (~ 1.48-7.68%) associated with further deoxygenation of graphene oxide framework. The most significant weight loss about (23-48%) was observed between (~700-998 °C) indicating combustion of carbon framework and possible sintering of metal oxide.

The Fe_2O_3/ZrO_2-GO catalyst demonstrated the highest thermal resistance, retaining 71% mass at 886°C. This superior thermal stability is attributed to the strong anchoring of Fe_2O_3 nanoparticles on the ZrO_2-GO support and the protective effect of the ZrO_2 layer, which retards carbon oxidation. The thermal resistance followed the order:

$$Fe_2O_3/ZrO_2\text{-GO} > NiFe_2O_4/ZrO_2\text{-GO} > NiO/ZrO_2\text{-GO} > ZrO_2\text{-GO}$$

Overall, the catalysts demonstrated excellent thermal resistance up to 400 °C, making them suitable for catalytic deoxygenation reaction typically conducted between 320-370 °C.

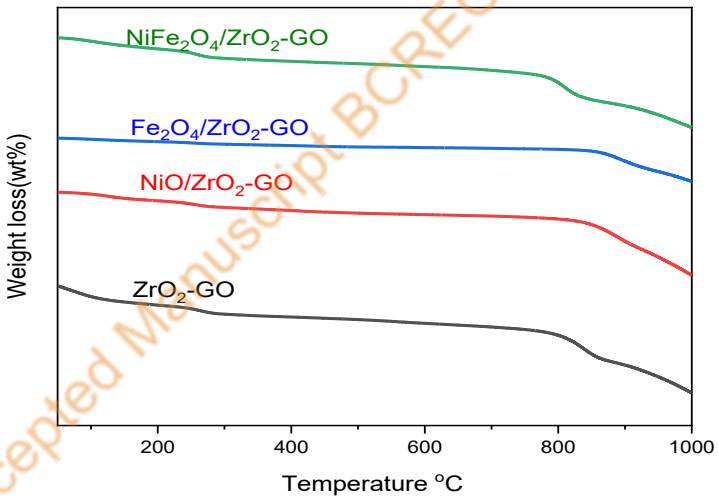

Figure 6. TGA analysis for new catalysts.

3.2 Catalytic deoxygenation activity for new catalysts

3.2.1 Gas Chromatography-Flame Ionization Detector (GC-FID) analysis

The catalytic performance of all ZrO_2-GO supported catalysts in the DO of palm oil was evaluated by GC-FID (Figure 7). The results demonstrate significant differences in HC%, kerosene yield, and Bio-jet fuel selectivity across the catalyst series. The performance followed the order:

HC% and kerosene yield:

Fe_2O_3/ZrO_2-GO > $NiFe_2O_4/ZrO_2$-GO > ZrO_2-GO > NiO/ZrO_2-GO

Bio-jet fuel selectivity:

$NiFe_2O_4/ZrO_2$-GO > ZrO_2-GO > Fe_2O_3/ZrO_2-GO > NiO/ZrO_2-GO

The superior performance of Fe_2O_3/ZrO_2-GO (HC% = 98%, kerosene yield = 86%, BJF selectivity = 40%) can be explained by the convergence of three key physicochemical factors. First, its high BET surface area (18.64 m^2/g) and pore volume (0.027 cm^3/g) maximize the number of accessible Fe^{3+} active sites and facilitate efficient intraparticle diffusion of bulky triglyceride molecules. Second, the small crystallite size (17.8 nm) of Fe_2O_3 ensures a high density of surface-active sites per unit mass of catalyst. Third, the moderate surface basicity (3234.65 µmol/g, distributed across weak, moderate, and strong sites) optimally steers the DO reaction toward DCO_2/DCO pathways, producing C_{15} and C_{17} hydrocarbons while minimizing cracking to lighter fractions. The Fe^{3+} species in hematite (α-Fe_2O_3) are well-established active sites for deoxygenation, facilitating C- bond activation through a redox mechanism in which Fe^{3+} is reduced to Fe^{2+} and reoxidized by the released CO_2/CO [38-40].

The inferior performance of NiO/ZrO_2-GO (HC% = 90%, kerosene yield = 60%, BJF selectivity = 35.5%) is mechanistically linked to its combination of low surface area (7.14 m^2/g) and excessively high basicity (7273.3 µmol/g). The former restricts the accessibility of active sites and hinders diffusion of large triglyceride molecules, while the latter promotes undesired side reactions including cracking, and isomerization that reduce selectivity toward diesel range hydrocarbons [38,39]. This demonstrates that catalytic performance in DO is not governed solely by the number of active sites but critically depends on their spatial distribution and the acid–base balance of the catalyst surface.

Compared with previously reported systems, Fe_2O_3/ZrO_2–GO demonstrates markedly superior performance. The Fe/HMS catalyst achieved 81.4% conversion and 96.4% C_8–C_{18} selectivity at 380°C [38], while Fe/AC showed only 55% HC yield and 52% alkane selectivity in palmitic acid DO at 450°C [39] both surpassed by Fe_2O_3/ZrO_2–GO at lower temperature of 350°C. The NiO–MoO_2/CeO_2 catalyst delivered ~77% HC yield at 15 wt% loading and 300°C [40], compared to 98%

achieved here at only 5 wt% loading. The superior performance of Fe_2O_3/ZrO_2-GO over these benchmarks is attributed to the synergistic effect of the ZrO_2-GO bifunctional support, which simultaneously provides high surface area, structural stability, and optimal surface basicity.

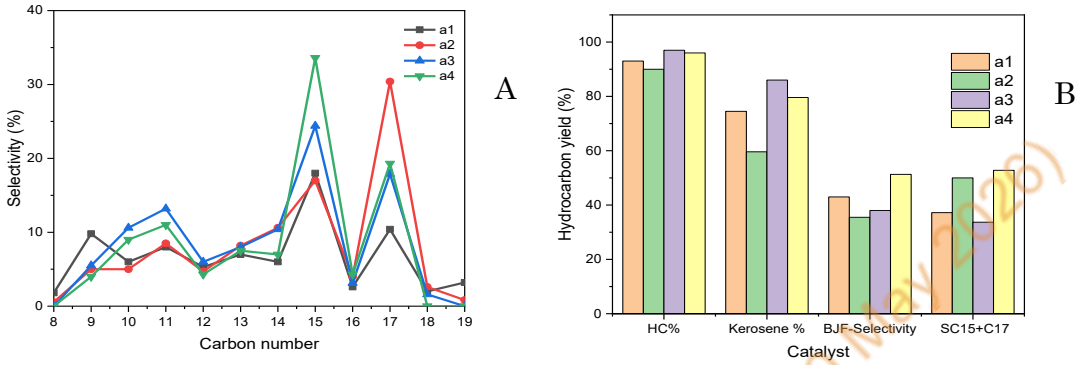

Figure 7. (A) carbon selectivity of deoxygenated product for (a1) ZrO_2-GO (a2) NiO/ZrO_2-GO (a3) Fe_2O_3/ZrO_2-GO (a4) $NiFe_2O_4/ZrO_2$-GO catalysts (B) HC %, kerosene %, BJF and $S_{C15+C17}$ selectivity for catalysts.

3.2.2 Gas Chromatography - Mass spectroscopy GC-MS

The GC-MS analysis (Figure 8) provided detailed compound distributions in the deoxygenated liquid products. Fe_2O_3/ZrO_2-GO achieved the highest alkane and alkene fraction (90%) with minimal oxygenated species (10%, including aromatics, ketones, and acids). The predominance of odd-carbon hydrocarbons (C_{15}, C_{17}) in the product distribution is consistent with DCO_2/DCO as the dominant pathway, in which the carboxyl carbon of fatty acids is removed as CO_2 or CO, yielding alkanes one carbon shorter than the parent fatty acid. This pathway preference is consistent with the moderate basicity of Fe_2O_3/ZrO_2-GO, which activates the C-O bond while retaining selectivity toward paraffins [41,42].

In contrast, the ZrO_2-GO support alone produced the lowest HC% (80%) with the highest oxygenated content (20%), attributable to its relatively high basicity (6018.42 µmol/g) promoting undesirable condensation and retarding complete C-O bond cleavage. The presence of oxygenates in the product confirms that strong basic sites alone, without appropriately dispersed metal active phases, are insufficient for complete deoxygenation.

3.2.3 Optimization of deoxygenation reaction conditions

Reaction conditions for Fe_2O_3/ZrO_2-GO were optimized using the OVAT approach, varying temperature (270-370 °C), reaction time (2-6 h), and catalyst loading (1, 3, 5, 7, and 10 wt%) under N_2 atmosphere at 400 rpm. The optimal conditions were identified as: temperature = 350 °C, reaction time = 3 h, and catalyst loading = 5 wt%, yielding HC% = 98% and kerosene yield = 86%. At temperatures below 350 °C, incomplete deoxygenation was observed due to insufficient thermal energy for C-O bond activation. Above 350 °C, cracking of the hydrocarbon products became increasingly significant, reducing selectivity toward diesel-range fractions. Similarly, catalyst loadings above 5 wt% did not further improve yield, likely due to mass transfer limitations at higher solid fractions, while excess catalyst promoted secondary cracking reactions.

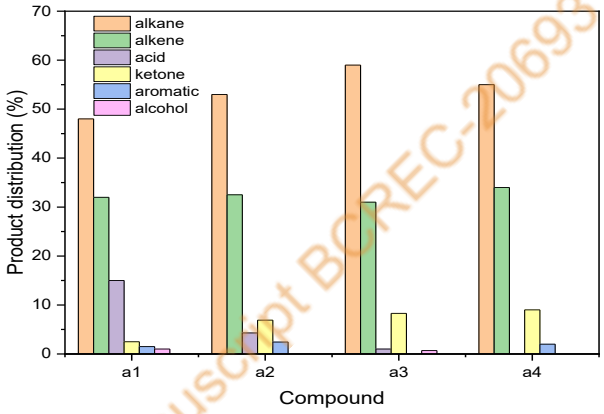

Figure 8. The liquid product Distribution of new catalysts.

3.2.4 Reusability and stability of optimal catalyst

The reusability of the Fe_2O_3/ZrO_2-GO catalyst was evaluated over four consecutive DO cycles under optimized conditions (Figure 9A–B). The catalyst retained 92% HC yield after four cycles, demonstrating excellent stability and reusability. A moderate decline in kerosene yield (from 86% to 80.9%) was observed alongside an increase in BJF selectivity (from 40% to 84%), reflecting a gradual shift in product distribution toward lighter BJF-range hydrocarbons (C_{11}-C_{15}). This shift is consistent with minor progressive changes in pore structure across repeated cycles, which is common behavior in heterogeneous catalysts operating under high-

temperature conditions and does not significantly compromise the overall catalytic performance.

Post-reaction characterization confirmed that the catalyst largely retained its structural integrity across four cycles. BET analysis showed a reduction in surface area from 18.64 m^2/g to 2.023 m^2/g and a decrease in pore volume from 0.027 to 0.016 cm^3/g after four cycles, accompanied by an increase in average pore size from 4.305 to 10.65 nm. These changes are attributable to partial coke deposition within the pore network and are typical of carbon-supported catalysts under prolonged high-temperature operation. Importantly, despite these textural changes, the catalyst retained 92% HC yield, confirming that the active Fe_2O_3 phase and the ZrO_2-GO support framework remain sufficiently intact to sustain high catalytic activity.

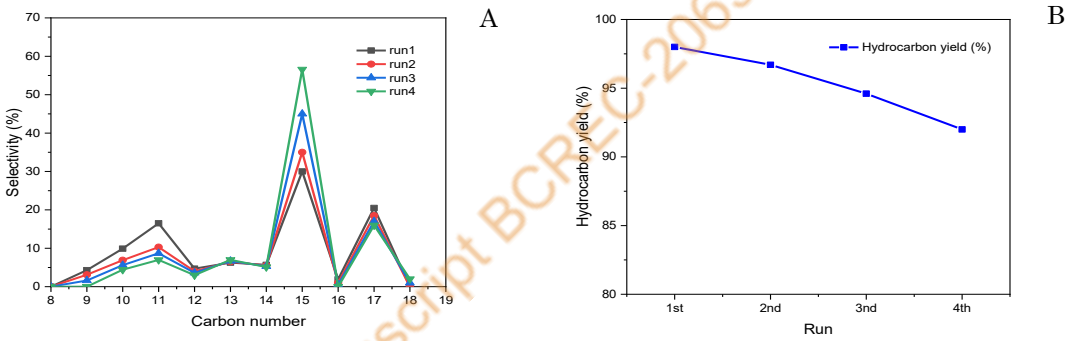

Figure 9. (A) Carbon distribution product on reusability study, (B) Hydrocarbon yield on 4th run.

Post-reaction XRD and TEM analyses further confirmed that the overall crystalline structure of the catalyst was preserved after four cycles, with only minor evidence of phase evolution. XRD patterns (Figure 10) showed slightly sharper peaks at 30.3°, 35.5°, 43°, 57°, and 63°, suggesting a degree of crystallite ordering consistent with mild thermal annealing rather than severe sintering.

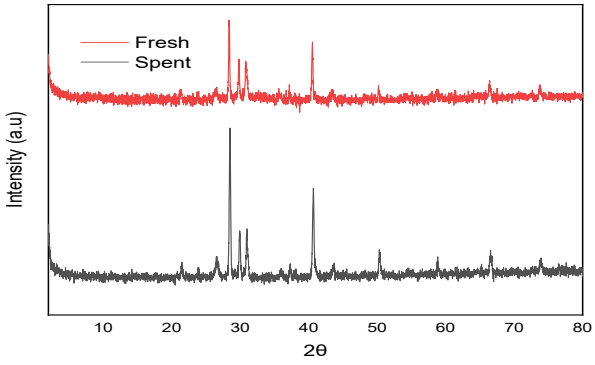

Figure 10. XRD pattern for the fresh and spent Fe_2O_3/ZrO_2-GO catalyst.

The N_2-adsorption /desorption isotherm of Fe_2O_3/ZrO_2-GO catalyst before and after four catalytic reaction cycles are illustrated in Figure. 11. Both fresh and spent catalysts showed Type-IV isotherm based on IUPAC classification, which indicate to mesoporous material with slit-like pore and aggregated plate-like particles typical of graphene-based support.

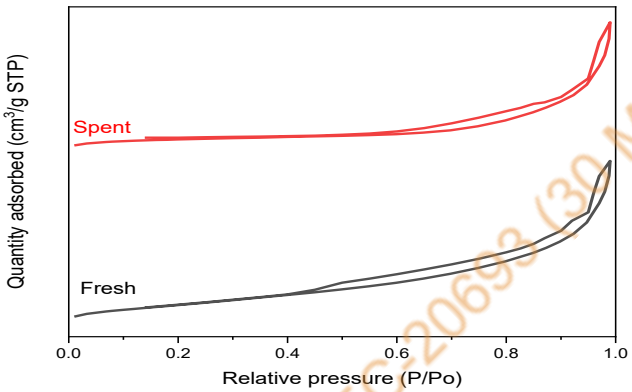

Figure 11. Isotherm linear plot for Fe_2O_3/ZrO_2-GO (spent and fresh catalysts).

TEM imaging (Figure 12) revealed some increase in nanoparticle size (to 30-56 nm), which is reasonable considering the repeated exposure to reaction temperatures of 350 °C, and the GO support sheets remained largely intact with only partial restacking observed. Overall, the Fe_2O_3/ZrO_2-GO catalyst demonstrated commendable durability, maintaining high performance across four consecutive reaction cycles, which underscores its practical potential as a stable and reusable catalyst for green diesel and bio-jet fuel production from palm oil.

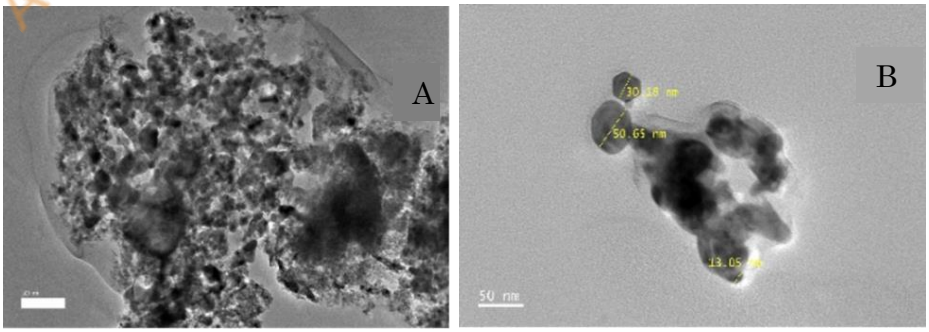

Figure 12. TEM image of a) fresh, and b) spent Fe_2O_3/ZrO_2-GO catalyst

4. Conclusion

This study successfully demonstrated the solvent-free production of bio-jet fuel and green diesel hydrocarbons through catalytic deoxygenation of palm oil over ZrO_2-GO-supported mono- and bimetallic oxide catalysts. Among the catalysts evaluated (ZrO_2-GO, NiO/ZrO_2-GO, Fe_2O_3/ZrO_2-GO, and $NiFe_2O_4$/ZrO_2-GO), the Fe_2O_3/ZrO_2-GO catalyst demonstrated superior performance, achieving 98% hydrocarbon yield and 86% kerosene yield under optimized conditions (5 wt% catalyst, 350 °C, 3 h, N_2 atmosphere). The exceptional activity is attributed to the synergistic combination of high BET surface area (18.64 m^2/g), large pore volume (0.027 cm^3/g), fine Fe_2O_3 crystallite dispersion (17.8 nm), and moderate surface basicity (3234.65 μmol/g). These properties collectively optimize mass transfer, maximize active site accessibility, and direct the DO reaction toward selective DCO_2/DCO deoxygenation pathways while suppressing cracking. The catalyst demonstrated remarkable stability over four consecutive cycles (92% HC yield retained), with deactivation attributed to coke deposition, sintering, and structural degradation of the GO support, as confirmed by post-reaction BET, XRD, and TEM characterization. These findings establish Fe_2O_3/ZrO_2-GO as a promising, low-cost catalyst for sustainable aviation fuel and green diesel production from palm oil and highlight the potential of ZrO_2-promoted graphene oxide as a bifunctional support for deoxygenation catalysis.

CRediT author statement

Attared F. Hassan: Conceptualization, Methodology, Formal analysis, Writing - Original draft. **Faris A. J. Al-Doghachi**: Supervision, Resources, Project administration. **Hassan T. Abdulsahib**: Formal analysis, Validation. **Yun Hin Taufiq-Yap**: Resources.

References

[1] Pratama, J. H., Rahmawati, Z., Widyanto, A.R., Gunawan, T., Abdullah, W., Jamari, N., Hamzah, A., Fansuri, H. (2024). Advancements in green diesel production for energy sustainability: a comprehensive bibliometric analysis. *Royal society of chemistry, 14, 36040-36062. DOI: 10.1039/d4ra06262k.*

[2] Zafeiropoulosa, J., Petropoulosa, G., Kordouli, E., Kordulis, C., Lycourghiotis, A., Bourikas, K. (2023). Development of nickel catalysts supported on silica for green diesel production. *Catalysis Today,* 423, 113952. *https://doi.org/10.1016/j.cattod..2022.11.013.*

[3] Kishore, S.C., Perumal, S., Atchudan, R., Sundramoorthy, A.K., Alagan, M.,

Sangaraju, S., Lee, Y.R. (2022). A Review of Biomass-Derived Heterogeneous Catalysts for Biodeisel Production. *Catalyst,* 12 1501; *https://doi.org/10.3390/catal 12121501.*

[4] Al-Doghachi F. A., Rashid, U., Taufiq -Yap, Y. H., (2016). Investigation of Ce(III) promoter e effects on the tri-metallic Pt, Pd, Ni/MgO catalyst in dry-reforming of methane. *RSC Advances*, 6, 10372; *DOI: 10.1039/c5ra25869c.*

[5] Wega Trisunaryanti, T. Triyono, Lip I. Fallah, Shafira Salsiah, Gesha D. Alisha. (2022). Highly Selective Bio-hydrocracking of Waste Palm Cooking Oil. *Bulletin of Chemical Reaction Engineering & Catalysis,* 17 (4), 712-724. *https://doi.org/10.9767/BCREC.17.4.15472.712-724.*

[6] Cao, Z., Yu, D., He, T., Li, T., Zuo, C., Hongbin Lv, B.L., Zheng, W., (2025). The Effect of Carbon Support on Ru/AC Catalysts Used for the Catalytic Decomposition of Hydroxylamine Nitrate and Hydrazine Nitrate. *Processes* 13(3), 641; *https://doi.org/10.3390/pr13030641.*

[7] Xiaobo, G., Peng, L., Jiaping, Z., Kui, W., Jianchun, J., Junming, X., (2025). Comparative Study of Ni-Fe Catalysts Loaded on Different Supports for Fatty Acid Hydrodeoxygenation. *Biomass and Bioenergy*, 202, 108242; *https://doi.org/10.1016/j.biombioe.2025.108242.*

[8] Guerrero-Corona, C. E., Melo-Banda, J. A., Lam-Maldonado, M., Vega-Ibarra, L. A., Diaz-Zavala, N. P., Meraz-Melo, M. A., (2024). Transition Metal Oxide Nano catalysts for Deoxygenation of Palm Oil to Green Diesel. *J. Frontiers in Chemical Engineering*; *Doi. 10.3389/fceng.2024.1334355.*

[9] William, N.P., Kevin, K.T., Marrcus, Y., Hansen, M., Jingguang, G.C., (2024). Transition metal nitride catalysts for selective conversion of oxygen-containing molecules. *Chemical Science*, 15(18): 6622-6642. *https://doi.org/10.1039/d4sc01314j.*

[10] Linyuan, Z., Huitu, Y., Xiangze, D., & Changwei, H., (2024). Regulating the Hydrodeoxygenation Activity of Molybdenum Carbide with Different Diamines as Carbon Sources, *Catalysts*, 14(2):138. *https://doi.org/10.3390/catal14020138.*

[11] Dahi, A., Sagar, B., Chi- Cong, T., Serge, K., & Samir H. M., (2023). Transition Metal Carbide Catalysts for Upgrading Lignocellulosic Biomass-derived Oxygenates: A review of the Experimental and Computational Investigations

into Structure-property Relationships, *Catalysis Today*, 423, 114285. *https://doi.org/10.1016/j.cattod.2023.114285.*

[12] Zhenping, C., Yongxin, D., Jiayin, Z., Panjie, Y., Yongde M., Yanning, C., Ying, Z., Kuan, H., & Lilong, J., (2023). In situ generation of dispersed MoS_2catalysts from oil-soluble MO-based ionic liquids for highly effective biolipids hydrodeoxygenation. *Journal of Catalysis,* 423, 50-61. *https://doi.org./10.1016/j.jcat.2023.04.022.*

[13] Napat, K., Masayoshi, F., & Apiluck, Eiad-Ua, (2022). Catalytic deoxygenation of palm oil over metal phosphides supported on palm fiber waste derived activated biochar for producing green diesel fuel, *RSC Advances,* 12,26051. *DOI: 10.1039/d2ra03496d.*

[14] Arun, N., Nanda, S., Hu, Y., 7 Dalai, A. K., (2021). Hydrodeoxygenation of oleic acid using γ-Al_2O_3 supported transition metallic catalyst systems: insight into the development on novel FeCu/γ-Al_2O_3 catalyst, *Molecular Catalysis*, *https://doi.org/10.1016/j.mcat.2021.111526.*

[15] Nugrahaningtyas, K. D., Mukhsin, S.A., Lukitawati, R., Rahmawati, F., (2025). A Series of Modified Mordenite for Green Fuel Production from Oleic Acid", *Sains Malaysia*, 54(8)): 1927-1944. *http://doi.org/10.17576/jsm-2025-5408-05* .

[16] Trisunaryanti, W., Triyono, Wijaya, K., Kartini, I., Purwono, S., Rodiansono, Mara, A., Dewi, A.I., (2024). Hydrodeoxygenation of refined palm kernel oil into bioavtur using spray-dry impregnated activated carbon supported-Mo catalysts", *Journal of Novel Carbon Resource Sciences & Green Asia Strategy",* 11(02), 652-664. *https://doi.org/10.1007/s11144-023-02560-3.*

[17] Afiqah-Idrus, A., Abdulkareem-Alsultan, G., Asikin-Mijan, N., Nassar, M.F., Voon, L., Teo, S. H., Kurniawan, T.A., Adzahar, N.A., Surahim, M., Razali, S.Z., Islam, A., Yunus, R., Alomari, N., (2024). Deoxygenation of waste sludge palm oil into hydrocarbon rich fuel over carbon-supported bimetallic tungsten-lanthanum catalyst. *Energy Conversion and Management: X,* 23 100589. *https://doi.org/10.1016/j,ecmx.2024.100589.*

[18] Al-Doghachi, F. A., Murad, D. M., Al-Niaeem, H. S., Al-Jaberi, S.H., Mohamad, S., Taufiq-Yap, Y.H., (2021). High Active Co/$Mg_{1-x}Ce_x^{3+}$ O Catalyst: Effects of Metal-Support Promoter Interactions on CO_2 Reforming of CH_4 Reaction. Bulletin of Chemical Reaction Engineering & Catalysis, 16(1), 97-110.

https://doi.org/10.9767/bcrec.16.1.9969.97-110.

[19] Zamani, A.S., Saidi, M., (2024). Green diesel alkanes production by hydrodeoxygenation of neem seed oil over nickel -zeolite based catalyst. *International Journal of Hydrogen Energy,* 29: 85-96. *https://doi.org/10.1016/j.ijhydene.2024.11.324.*

[20] Tang, K., Liu, X., Jiang, G., Zhang, Y., Meng, X., Lu, J., Zhang, H., Gao, Y., Qin, Z., Lin, F., (2025). Modulating oxygen vacancies to simultaneously promote Pd atom stability and O activation over Pd/CeO_2 catalysts for enhancing catalytic efficiency and durability", *CrystEngComm*. 27,4956-4964. *https://doi.org/10.1039/D5CE00381D.*

[21] Siraj, M., Ceylan, S., (2025). Investigation of the effect of catalyst support on oleic acid catalytic deoxygenation for green diesel production. *Journal of Porous Materials, https://doi.org/10.1007/s10934-024-01725-2.*

[22] Salehi, S., Alavi, S. M., Rezaei, M., Akbari, E., Varbar, M., (2024). Syngas production from dry reforming of glycerol by NiO/M-Al_2O_3 catalysts: Effect of Various support promoters and various ZrO_2 content. *Journal of CO_2 Utilization,* 81, 102737. *https://doi.org/10.1016/j.jcou.2024.102737.*

[23] Ferreira, K. K., Di Stasi C., Ayala-Cortes, A., Ribeiro, S., Pinilla, J.L., Suelves, I., Pereira, M. F., (2024). Hydroprocessing of waste cooking oil to produce liquid fuels over Ni-Mo and Co-Mo supported on carbon nanotubes. *Biomass and bioenergy,* 191, 2024, 107480. *https://doi.org/10.1016/j.biombioe.2024.107480.*

[24] Martina, P., Iryna, D., Ayesha S., Tomas, H., Mariia, K., Berke, S., Lukášny, K., Martin, V., (2025). Graphene oxide-supported metal catalysts for selective hydrogenation of cinnamaldehyde: impact of metal choice and support structure, *Catalysts,* 15(5)470. *https://doi.org./10.3390/catal15050470.*

[25] Sohail M., Saleem. M., Sana Ullah, Noor Saeed, Ayesha Afridi, Majid Khan, (2017). Modified and improved Hummer's synthesis of graphene oxide for capacitors applications. *Modern Electronic Materials,* S2452-1779(17)30031-2. *https://doi.org/10.1016/j.moem.2017.07.002* .

[26] Adzahar, N.A., Abdulkareem-Alsultan, G., Mijan, N. A., Mastuli, M.S., Lee, H. V., Taufiq-Yap, Y. H., (2024). Effect of catalyst synthesis of bimetallic nickel-cobalt supported iron-based catalysts on converting palm kernel oil into bio-jet

fuel via deoxygenation reaction. *Journal of Energy*. (314) 03735-6. *https://doi.org/10.1016/j.energy.2024.133957*.

[27] Bojarska, Z., Mazurkiewicz-Pawlicka, M., Makowski, L., (2019). Graphene oxide-based nanomaterial as catalysts for oxygen reduction reaction. *Chemical and Process Engineering,* 40(4), 361-376. *DOI: 10.24425/cpe.2019.130212*.

[28] A Smirnov, N W Pinargote, N Peretyagin, Y Pristinskiy, P Peretyagin and J F. Bartolomé. Zirconia Reduced Graphene Oxide Nano-Hybrid Structure Fabricated by the Hydrothermal Reaction Method. *Material,* 2020; *DOI:10.3390/ma13030687*.

[29] Al-Doghachi, F. A., Taufiq-Yap, Y. H., (2018). CO_2 Reforming of Methane over Ni/MgO Catalysts Promoted with Zr and La Oxides. *Chemistry Select*. *https://doi.org/10.1002/slct.201701883*.

[30] Haghoghi, S.M., Hemmati, A., Moghadam Zadeh, H., A., Raoofi N., (2024). Using NaOH @ graphene oxide- Fe_2O_3 as a magnetic heterogeneous catalyst for ultrasonic transesterification; experimental and modelling. *Scientific reports*. 22(14), 14386. *DOI; 10.1038/s41598-024-64865-0*.

[31] Al-Doghachi1, F.A. J., Islam,A., Zainal, Z., Saiman, M.I., Embong, Z., Taufiq-Yap, Y.H., (2016). High Coke-Resistance Pt/Mg1-xNixO Catalyst for Dry Reforming of Methane. *PLOS ONE*, *DOI; 10.1371/journal.pone.0145862*.

[32] Rehman, W., Saeed, F., Arain, S., Usman, M., Maryam, B., Liu, X., (2025). Enhanced photoelectrochemical water splitting using a $NiFe_2O_4$/NG@MIL-100(Fe)/TiO_2 composite photoanode: synthesis, characterization, and performance. *J. Compos. Sci.,* 9(5), 250. *https://doi.org/10.3390/jcs9050250*.

[33] Al-Doghachi, F.J., (2018). Effects of platinum and palladium metals on Ni/Mg1-xZrxO catalysts in the CO_2 reforming of methane. *Bulletin of Chemical Reaction Engineering & Catalysis*. 13(2), 295-310, 2018. *https://doi.org/10.9767/bcrec.13.2.1656.295-310*.

[34] Al-Jaberia, S. H., Rashid, U., Al-Doghachi, F. A., Abdulkareem-Alsultan, G., Taufiq-Yap, Y.H., (2017). Synthesis of MnO-NiO-SO_4^{-2}/ZrO_2 solid acid catalyst for methyl ester production from palm fatty acid distillate. *Energy Conversion and Management* ,139, 166-174. *https://doi.org/10.1016/j.enconman.2017.02.056*.

[35] Al-Doghachi, F.A., Al-Najar, A.M., Safa-Gamal, M., Taufiq-Yap, Y.H., (2023). Catalytic Dry-reforming of Methane Process with Co,Ni,Pd/Ca-La-O Mixed Oxides. *Bulletin of Chemical Reaction Engineering & Catalysis*. 18(4), 677. *https://doi.org/10.9767/bcrec.20053*.

[36] Wierzbicki, D., Debek, R., Motak, M., Grzybek, T., Galvez, M. E. & Costa, P. Da, (2016). Novel Ni-La-Hydrotalicite Derived Catalysts for CO_2 Methanation. *Catal. Commun*., 83, 5-8. *https://doi.org/10.1016/j.catcom.2016.04.021*

[37] Nugraha, R.E., Sunarti, Y., Tehubijuluw, H., Mumtazah, Z., (2022). Effect of catalytic properties on the deoxygenation reaction of vegetable oil and model compound to produce diesel range hydrocarbon fuels" A review. *Journal of Kimia Riset*. 7(1), 81-93. *DOI: 10.20473/jkr.v 7i1.35974*.

[38] Bian J. Wang Y. Zhang Q. Fang X. Feng L. Li C.2017, "Fatty acid decarboxylation reaction kinetics and pathway of co-conversion wiyh amino acid on supported iron oxide catalysts". RSC Adv.,7:47279-47287. *https://doi.org/10.1039/C7RA08507A*.

[39] Zulkepli S, Lee H V, Rahman N Abd, Chuan L T, Show P L, Chen W-H, Juan JC, 2022, "Highly active iron-promoted hexagonal mesoporous silica (HMS)for deoxygenation of triglycerides to green diesel hydrocarbon-like biofuel". *Fuel*. ,308:121860. *DOI: 10.1016/j.fuel.2021.121860*.

[40] Bian Z, Das S, Wai M H, Hongmanorom P, Kawi S, (2017), "A Review on ChemPhysChem,18(22), 3117-3134. *https://doi.org/10.1002/cphc.201700529*.

[41] Hart, A., Patel, H., Yildirir, E., Onwudili, J.A., (2025). Influence of surface acidity/basicity of selected metal oxide catalysts and reaction atmospheres on the ketonisation of propionic acid to produce 3-pentanone as a liquid biofuel precursor, *Renewable Energy*. 250, 123386. *DOI:10.1016/j.renene.2025.123386*.

[42] Zhou, L., Yang, H., Hu, C., (2025). Catalytic Deoxygenation of Lipids for Bio-Jet Fuel: Advances in Catalyst Design and Reaction Pathways. *Catalysts*. 15(6), 518.; *https://doi.org/10.3390/catal15060518*.